

Real-Space Mapping of Local Subdegree Lattice Rotations in Low-Angle Twisted Bilayer Graphene

Ya-Ning Ren,* Zhen Zhan, Yi-Wen Liu, Chao Yan, Shengjun Yuan, and Lin He*



Cite This: *Nano Lett.* 2023, 23, 1836–1842



Read Online

ACCESS |



Metrics & More



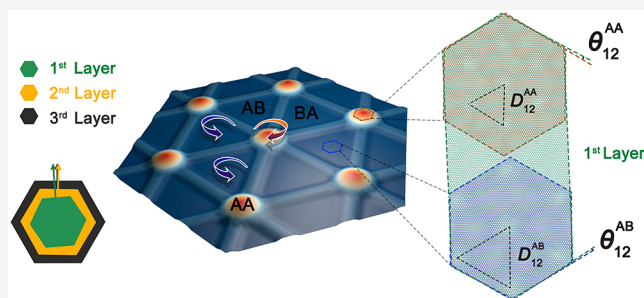
Article Recommendations



Supporting Information

ABSTRACT: In two-dimensional small-angle twisted bilayers, van der Waals (vdW) interlayer interaction introduces an atomic-scale reconstruction, which consists of a moiré-periodic network of local subdegree lattice rotations. However, real-space measurement of the subdegree lattice rotation requires extremely high spatial resolution, which is an outstanding challenge in an experiment. Here, a topmost small-period graphene moiré pattern is introduced as a magnifying lens to magnify sub-Angstrom lattice distortions in small-angle twisted bilayer graphene (TBG) by about 2 orders of magnitude. Local moiré periods of the topmost graphene moiré patterns and low-energy van Hove singularities of the system are spatially modified by the atomic-scale reconstruction of the underlying TBG, thus enabling real-space mapping of the networks of the subdegree lattice rotations both in structure and in electronic properties. Our results indicate that it is quite facile to study subdegree lattice rotation in vdW systems by measuring the periods of the topmost moiré superlattice.

KEYWORDS: twisted bilayer graphene (TBG), structure reconstruction, scanning tunneling microscopy (STM) and spectroscopy (STS), moiré magnifying lens



Stacking two-dimensional (2D) van der Waals (vdW) bilayers with a controlled interlayer twist angle provides a new pathway to engineer structures and electronic properties of the system with continuous tunability.^{1–5} However, recent studies demonstrate that the structures of the 2D vdW twisted bilayers could be distinct from that by assuming a rigid rotation of two adjacent layers.^{6–23} In 2D vdW twisted bilayers, vdW interlayer interaction can cause atomic-scale reconstruction at the vdW interfaces by favoring commensuration between the two adjacent layers, which competes with the intralayer elastic energy. Twisted bilayer graphene (TBG), as the most studied 2D vdW bilayers, exhibits substantial lattice reconstruction at the interface for small twist angle θ , significantly changing its lattice symmetry and electronic structure.^{11,12,15,21–23} The interfacial reconstruction in the TBG is achieved by locally rotating the lattice to form a moiré-period network of the rotations (the local lattice rotation is usually less than 1°). Recent developments in state-of-the-art microscopy techniques have enabled characterization of atomic-scale reconstruction in the TBG,²² but real-space measurement of the local subdegree lattice rotation requires extremely high spatial resolution and has remained an outstanding challenge in experiment.

Here, we demonstrate a general approach for real-space measurement of the local subdegree lattice rotation in the small-angle TBG by using a topmost large-angle (small-period) graphene moiré as a magnifying lens. The sub-Angstrom lattice distortions in the underlying small-angle TBG are magnified by about 2 orders of magnitude by the topmost moiré (see Figure

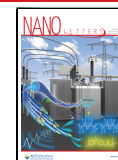
S1), resulting in the spatial modified twist angles of the topmost TBG and low-energy van Hove singularities (VHSs) of the system. These enable us to real-space map the networks of the subdegree rotations in the underlying TBG both in structure and in electronic properties. Because of the magnifying effect of the topmost moiré, it is possible to obtain the local subdegree lattice rotation by simply measuring the nanoscale periods of the topmost moiré pattern.

Figure 1a shows a schematic of a tiny-angle TBG with a large period of moiré superlattice. The interfacial reconstruction is expected to occur by two rotation modes at the AA stacking regions and the AB (BA) stacking regions. In the past few years, many efforts have been made to measure the atomic reconstruction in the tiny-angle TBG. However, only very recently, the displacement fields and the localized subdegree lattice rotations of the TBG were measured by using a newly developed Bragg interferometry, based on four-dimensional scanning transmission electron microscopy.²² In this work, we demonstrate that it is possible to real-space map the local subdegree lattice rotations by introducing another large-angle

Received: December 1, 2022

Revised: February 14, 2023

Published: February 17, 2023



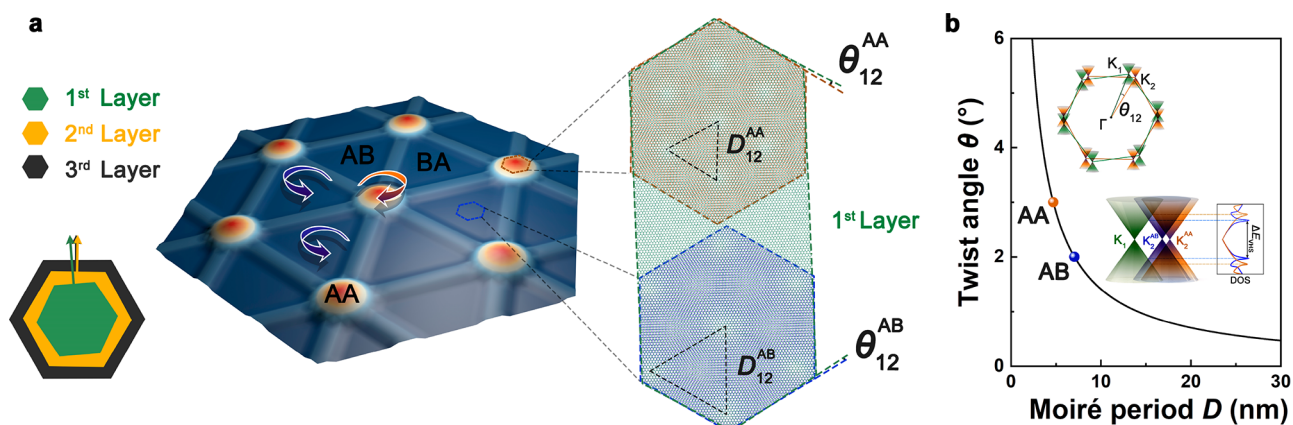


Figure 1. Schematic view of local lattice rotation magnified by a topmost moiré. (a) Left panel: The sketch of a TTG. Middle panel: Schematic of the moiré pattern for underlying tiny-angle TBG. Right panel: Simulated images of local twist angles between the first and the second layer. (b) Twist angle as a function of the moiré period. The insets show the first Brillouin zone and the electronic band structure of TBG. K_1 and K_2 are the Dirac points of two layers. The overlap of the two Dirac cones, K_1 and K_2^{AA} (or K_2^{AB}), generates two peaks in the DOS.

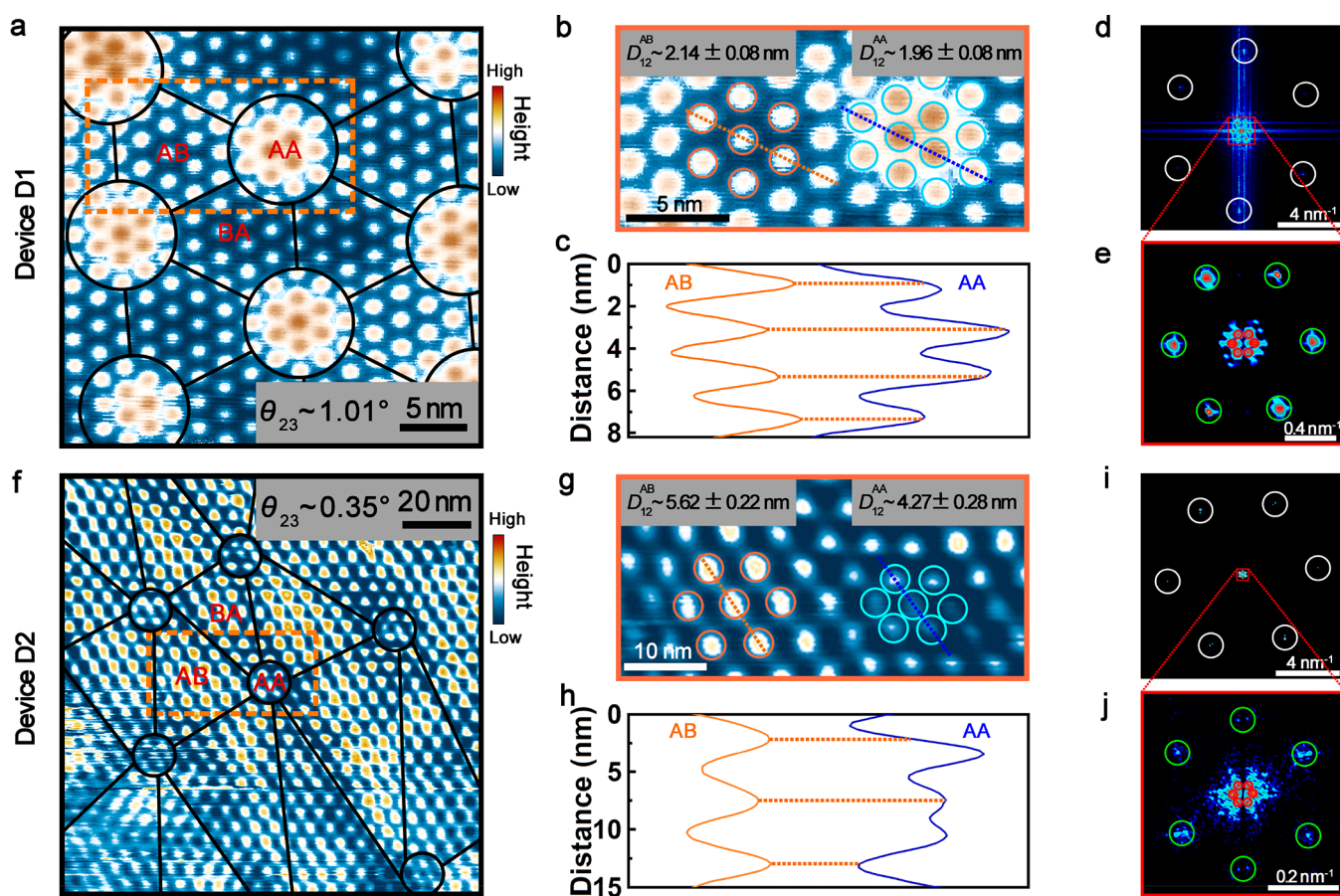


Figure 2. Structure characterization of the TTG. (a,f) STM topographies showing the “double-moiré” superlattices on two TTG samples. Topographies were taken at 1 V and 200 pA, and at 0.25 V and 400 pA, respectively. The overlaid circles and lines depict the moiré structure in the underlying TBG. (b,g) STM images within the orange frame in (a,f), respectively. The profile lines along the dashed lines are shown in (c,h). (d,e) Corresponding FFT images of device D1. (i,j) Corresponding FFT images of device D2. The white circles in (d,i) show reciprocal lattices of graphene. The green circles in (e,j) show the reciprocal moiré superlattices of the topmost bilayer, and the red circles in (e,j) show the reciprocal moiré superlattices of the underlying bilayer.

graphene moiré as a magnifying lens (see Figure S1).^{24–26} By adding a graphene sheet on top of the tiny-angle TBG with a large twist angle, the studied system becomes twisted trilayer graphene (TTG) with a small period moiré generated between the first and the second layer D_{12} , and a large period moiré

generated between the second and the third layer D_{23} (Figure 1a). The periods of moiré pattern D generated between the topmost layer and the second layer at the AA and the AB (BA) stacking regions, labeled as D_{12}^{AA} and D_{12}^{AB} (D_{12}^{BA}) respectively, should be quite different because of the local lattice rotation of

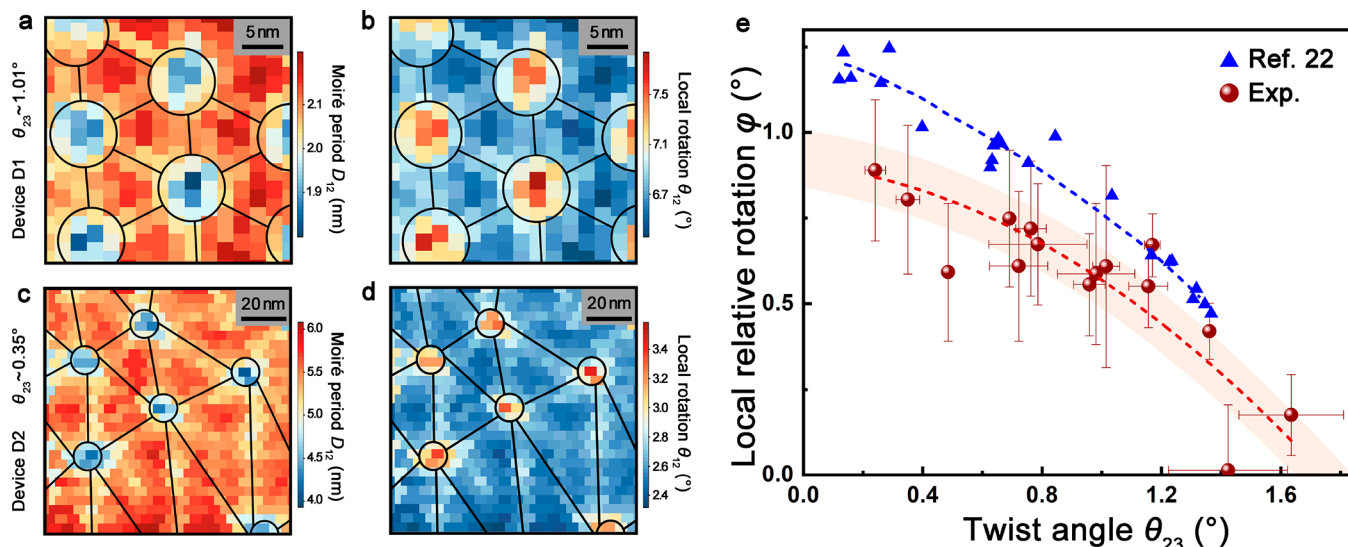


Figure 3. Real-space map of the local lattice rotation magnified by a topmost moiré. (a,c) The moiré period D_{12} in the devices D1 and D2 as a function of positions. (b,d) The spatial variations of the θ_{12} . The overlaid circles and lines in (a–d) depict the moiré structure in the underlying TBG. (e) Red solid dots show the measured averaged ϕ as a function of θ_{23} on different devices. The error bars reflect the standard error of the data. Blue solid triangles are the local relative lattice rotation between the AA and AB regions as a function of θ_{23} , adapted from Figures 3f and 3h in ref 22.

the tiny-angle TBG (Figure 1a). We can obtain the local twist angles at the AA and the AB (BA) stacking regions, labeled as θ_{12}^{AA} and θ_{12}^{AB} (θ_{12}^{BA}) respectively, based on the measured periods D_{12}^{AA} and D_{12}^{AB} (D_{12}^{BA}) according to $D = a/[2\sin(\theta/2)]$, where $a \approx 0.246$ nm (Figure 1b).^{27–31} Then, the difference between the θ_{12}^{AA} and θ_{12}^{AB} (θ_{12}^{BA}) directly reflects the local relative rotation ϕ between the AA and the AB (BA) stacking regions in the tiny-angle TBG.

To realize the above measurements, the global twist angle between the topmost layer and the second layer, labeled as θ_{12} , should be large enough to ensure that the period of the moiré pattern is much smaller than the size of the AA stacking region in the underlying tiny-angle TBG. Another advantage of the large twist angle is that it depends extremely sensitively on the period of the moiré pattern (Figure 1b), which ensures more accurate measurement. In our work, the experiments are carried out on transferred TTG (see Figure S2) on 0.7% Nb-doped SrTiO₃, as reported in ref 21, by using scanning tunneling microscopy/spectroscopy (STM/STS). In our TTG, the global twist angle between the second layer and the third layer, labeled as θ_{23} , ranges from 0.24° to 1.6°, and the θ_{12} is usually larger than 2°. Figure 2 shows representative STM measurements of two TTG. Both samples can be identified by the characteristic “double-moiré” superlattices of the TTG,^{32–34} according to both the STM images (Figure 2a,f) and their corresponding fast Fourier transform (FFT) images (Figure 2d,e,i,j). In the TTG, the large-period moiré patterns shown in Figure 2a,f are generated by the twist angle $\theta_{23} \approx 1.01^\circ \pm 0.05^\circ$ (device D1) and $0.35^\circ \pm 0.04^\circ$ (device D2) respectively. In the tiny-angle TBG, even minor local heterostrain variations lead to large changes ($\sim 1/\theta$) in the moiré periodicity.^{12,23} Therefore, we observe more pronounced irregular moiré patterns in the device D2 TTG ($\theta_{23} \approx 0.35^\circ$).

Besides the “double-moiré” superlattices, the most pronounced feature observed in the STM images of the TTG is that the periods of the topmost moiré pattern D_{12} vary at different positions (Figure 2a,f; see Figures S3 and S4 for more

STM characterizations). For example, $D_{12}^{AA} \approx 1.96 \pm 0.08$ nm and $D_{12}^{AB} \approx 2.14 \pm 0.08$ nm in the device D1 (Figure 2b,c), which indicate $\theta_{12}^{AA} \approx 7.21^\circ \pm 0.29^\circ$ and $\theta_{12}^{AB} \approx 6.60^\circ \pm 0.25^\circ$, suggesting a local lattice rotation between the AA and AB regions (see Figure S5 for method of measuring the moiré periods). The twist angle θ can also be roughly measured according to the FFT of the STM images, and both methods obtain the consistent result (see Figure S6 for method of measuring the twist angle according to the FFT image).^{27–30,35} Similarly, we obtain $D_{12}^{AA} \approx 4.27 \pm 0.28$ nm ($\theta_{12}^{AA} \approx 3.32^\circ \pm 0.22^\circ$) and $D_{12}^{AB} \approx 5.62 \pm 0.22$ nm ($\theta_{12}^{AB} \approx 2.51^\circ \pm 0.10^\circ$) in the device D2 (Figure 2g,h). For the TBG with a large twist angle, the size of the moiré pattern is quite small, and the rigid structure is energetically preferable. To confirm this, we carry out atomic-resolved STM measurement of the lattice structure of the top layer, which indicates that there is no comparable reconstruction and detectable strain in the top layer, i.e., the top layer sits rigidly on top of the studied structure (see Figure S4 for details). The semiclassical molecular dynamics simulation method is used to study full lattice relaxation of the system. Our simulation indicates that the topmost layer has a minor influence on the lattice relaxation of the second and third layers and the topmost layer can be approximately regarded as a rigid structure when the twist angle between the topmost layer and the second layer are relatively large (see Figure S24 for details). Hence, the periods of the moiré pattern should be a constant. Therefore, the observed spatial variation of the moiré D_{12} is attributed to the local lattice rotation in the underlying small-angle TBG, as illustrated in Figure 1.

To further explore effects of the local lattice rotation on the structure of the topmost TBG, we measure the moiré periods D_{12} in the two exemplary TTG samples ($\theta_{23} \approx 1.01^\circ$ and 0.35°) as a function of positions, as shown in Figure 3a,c, respectively. Obviously, the measured results exhibit the same feature of a moiré pattern in the underlying TBG, which provides direct experimental evidence that the spatial variation of the D_{12} arises from the structural reconstruction in the underlying TBG. According to $D = a/[2\sin(\theta/2)]$, the spatial

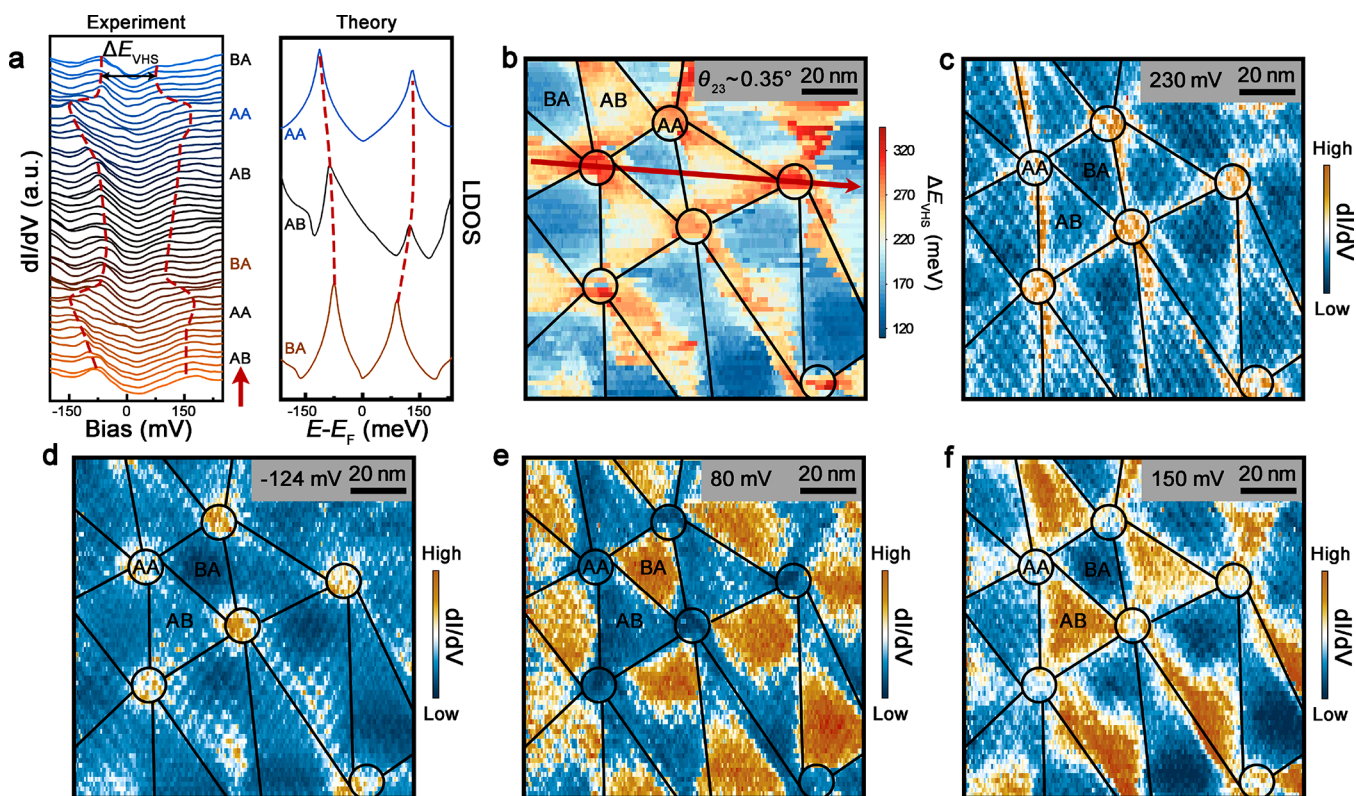


Figure 4. Spatial variation of electronic properties induced by the structure reconstruction in TBG. (a) The experimental (left panel) and theoretical (right panel) dI/dV spectra along the arrow in device D2 in panel (b). (b) Map of the ΔE_{VHS} in the topmost TBG, plotted according to 13160 spectra recorded at different positions. (c–f) STS maps of the $\theta_{23} \approx 0.35^\circ$ TTG with the fixed sample bias, i.e., 230, –124, 80, and 150 mV, respectively (tunnel current $I = 400$ pA). The overlaid circles and lines depict the moiré structure in the underlying TBG.

distributions of the θ_{12} in the two TTG samples are plotted in Figure 3b,d. Generally, the θ_{12}^{AA} is larger than the θ_{12}^{AB} (θ_{12}^{BA}) and $\theta_{12}^{AB} \approx \theta_{12}^{BA}$, which are consistent with the reconstruction mechanism predicted by theoretical studies.^{7–9} The moiré superlattice magnifies the local lattice rotation of the networks and allows us to measure it with standard STM measurement. Actually, even the atomic resolution is unnecessary to measure the subtle local lattice rotation. Based on the results in Figure 3b,d, we can also obtain the local relative lattice rotation in the triangular network of the domain walls (DWs) θ_{12}^{DW} , and generally, we obtain $\theta_{12}^{AA} > \theta_{12}^{DW} > \theta_{12}^{AB}$ ($\approx \theta_{12}^{BA}$). Our experiment also indicates that there is local strain in the second/third layer of several studied samples, which results in anisotropy of the large moiré period (see Figure 2f as an example). Then, there is a slight spatial variation of the small moiré period generated between the first and the second graphene layer in the AB regions of the second and the third layer (see Figure 3c as an example). This can slightly vary the obtained local rotation angle (see Figure 3d). However, such a result does not affect the main feature of the spatial variation of the local rotation angle, see Figure 3b,d for comparison. Similar measurements were carried out in 15 TTG with different θ_{23} values, ranging from 0.24° to 1.6° (see Supporting Information Figures S7–S12), and we generally obtain $\theta_{12}^{AA} > \theta_{12}^{DW} > \theta_{12}^{AB}$ ($\approx \theta_{12}^{BA}$) for all the studied samples. Figure 3e summarizes the averaged local relative lattice rotation between different AA and AB regions, defined as $\varphi = \theta_{12}^{AA} - \theta_{12}^{AB}$, as a function of θ_{23} based on the measurements of the 15 TTG. For comparison, the result obtained in ref 22 is also plotted. Both results reveal quantitatively a similar trend in the amplitude of the local

lattice rotation: as the θ_{23} nears zero, the φ approaches a limiting value of approximately 1.0° . Extrapolation of φ to large θ_{23} indicates that the onset of reconstruction begins below about 1.7° .

The local lattice rotation in the underlying tiny-angle TBG not only leads to spatial variation of the twist angles but also results in spatial modulated electronic properties of the system. The twist angle determines the momentum separation, $\Delta K = 2|K|\sin(\theta/2)$, of the two Dirac cones (K_1 and K_2) between the adjacent graphene layers (here $|K| = 4\pi/3a$), as schematically shown in inset of Figure 1b for the TBG. A finite interlayer coupling t_θ generates a pair of saddle points, which introduce two pronounced VHSs with the energy separations ΔE_{VHS} in the density of states (DOS).^{4,5,27–31} Therefore, the spatial variation of the θ_{12} is expected to lead to spatial modulation of the VHSs. To explore this effect, we carry out STS measurements in the TTG and two low-energy VHSs emerge in the STS spectrum (see Figure S13 for method in determining the ΔE_{VHS}). In our experiment, the interlayer coupling in the topmost TBG is stable³⁶ and the ΔE_{VHS} is independent of the measured time (Figure S14). The heterostrain in the topmost TBG is almost negligible and is not expected to affect the measured ΔE_{VHS} (see Figure S15).^{37–39} According to the result in Figure 4a (left panel), the ΔE_{VHS} depends sensitively on the measured positions. To further understand the electronic properties of the system, we carry out band structure calculations for bilayer and trilayer graphene in different stacking configurations. Our calculations indicate that only considering electronic structures of the topmost bilayer cannot consistently explain the observed

ΔE_{VHS} in different regions, especially the difference between the values of ΔE_{VHS} in the AB and BA regions (see Figure S16). However, by taking into account the stacking orders of the three layers, our calculation can reproduce well the spatial variation of the ΔE_{VHS} observed in experiment, as shown in Figure 4a (right panel) (see Figure S17 for details). Figure 4b shows the spatial variation of the ΔE_{VHS} measured in the device D2 (see Figures S18 and S19 for more experimental data). Obviously, the spatial variation of the ΔE_{VHS} exhibits the same structure of the moiré pattern in the underlying TBG, demonstrating explicitly that the electronic properties of the system are strongly modified by the structural reconstructions in the underlying TBG. Because the twist angle between the first/second layers is large, the electronic structures and local density of states are almost independent of positions in both the AB and BA regions (see Figure S20), which are distinguished from the large-area trilayer graphene with different stacking orders (see Figure S21). However, the substrate and the STM tip can generate an effective electric field on the AB and BA regions and break their symmetry,^{23,40–42} which may slightly affect the values of ΔE_{VHS} in the two regions. For the sake of simplicity, we applied a vertical electric field to the AB region, and the calculated values of ΔE_{VHS} in the three regions can be roughly consistent with our experiment. According to the result in Figure 4b, there are other features that cannot be simply explained by the structural reconstruction in the underlying TBG. Our experiment also indicates that the local heterostrain in the underlying TBG can affect the spatial variation of the ΔE_{VHS} , as shown in bottom of Figure 4b showing the region with a large anisotropy of the moiré periodicity. Such a result is reasonable because the heterostrain of tiny-angle TBG can lead to a tetragonal structural transition in the moiré pattern, even resulting in a missing DW that separates the AB and BA regions.^{12,21,23}

By carrying out energy-fixed STS mapping at different energies, as shown in Figure 4c–f, we can clearly observe effects of the interfacial reconstruction in the underlying TBG on the electronic properties. The spatial variations of the VHSs in the topmost TBG induced by the underlying interfacial reconstruction are shown in Figure 4d–f, which agree quite well with the STS spectra shown in Figure 4a. Such a result demonstrated explicitly that the interfacial reconstruction in the underlying TBG leads to the spatial variations of the VHSs. In our experiment, the measured size of the AA stacking regions in the underlying bilayer is almost the same as that obtained in the TBG of ref 22, which further confirms that the relaxation within the underlying bilayer is almost independent of the topmost layer (see Figure S22). In the STS measurement, besides the two VHSs, two new peaks only localized in the DW are observed in the spectra (see Figure S23). Our energy-fixed STS map indicates that the new peak is strongly localized in the triangular DWs, as shown in Figure 4c. These features remind us of the predicted DW modes (pseudo-Landau levels) at the interfaces of AB and BA regions in the tiny-angle TBG.⁴³ However, because of the structural reconstruction in the tiny-angle TBG, the highly localized pseudo-Landau levels form a triangular network connecting different AA regions, rather than the predicted Kagome lattice with assuming a rigid rotation of two adjacent layers, as observed very recently.²³

In summary, by using the magnifying effect of the topmost small-period graphene moiré, we realize real-space measurement of the local subdegree lattice rotations of small-angle

TBG. The subdegree lattice rotation in the underlying small-angle TBG spatially modifies twist angles of the topmost small-period graphene moiré and low-energy VHSs of the system, which enable us to real-space measure the local rotation networks both in structure and electronic properties. Our results provide a general method to study the structural reconstruction in the vdW systems by using the moiré superlattice as a magnifying lens. A general criterion is that the top layer has weak coupling and a small lattice constant difference with the underlying bilayer.

METHODS

Preparation of Samples. The graphene was synthesized on a 25- μm -thick nickel foil (purchased from Alfa Aesar) via a low-pressure chemical vapor deposition (LPCVD) method. Figure S2 shows the growth process. The nickel foil was first heated from room temperature to 1000 °C in 40 min under a H_2 flow of 50 sccm (standard cubic centimeter per minute) and an Ar flow of 50 sccm in a horizontal tube furnace (Xiamen G-CVD system). Then, the temperature and gas environment were kept for 20 min. Next, 20 sccm CH_4 was introduced to the system for 15 min as carbon source for the growth of graphene. Finally, the sample was cooled down to room temperature.

Transfer of Graphene Sheets. The as-grown graphene film was transferred onto an annealed 0.7% Nb-doped SrTiO_3 substrate by the PMMA-assisted method using the transfer platform from Shanghai Onway Technology Co., Ltd. First of all, spin-coated poly(methyl methacrylate) (PMMA) film onto the graphene surface at 180 °C for 3 min. Next, the sample was immersed into the FeCl_3 solution to etch the nickel away, so the PMMA/graphene film was detached from the nickel foil. After that, we used ultrahigh-purity water to clean it for hours, then transferred the PMMA/graphene membrane onto a SrTiO_3 substrate (was annealed in ultrahigh-vacuum (UHV) chamber at ~ 1200 °C for ~ 30 min to obtain large terraces) before it dried in air for hours. Finally, the PMMA was removed in CVD vacuum at 550 °C for 6 h under an Ar flow of 50 sccm and a hydrogen gas flow of 50 sccm. Then, the sample was inserted into the UHV chamber and was annealed at 200–300 °C for ~ 10 min to remove airborne adsorbates from the surface. After that, the samples are directly studied by using STM. There are large-area terraces in the annealed 0.7% Nb-doped SrTiO_3 substrate, which are important to measure structures and electronic properties of large-area twisted trilayer graphene (TTG). Due to the twist tendency between adjacent layers of the synthesized graphene, it is easy to find TTG with different twist angles to carry out the experiment. In our experiment, we carried out measurements on 15 different TTG samples. In these TTGs, the period of the moiré pattern generated between the topmost layer and the second layer is much smaller than the size of the AA stacking region between the second layer and the third layer; thus, the local lattice rotation in the underlying TBG can be magnified by the topmost moiré superlattice.

STM and STS Measurements. STM/STS characterizations were performed with a low-temperature (~ 4.2 K) ultrahigh-vacuum ($\sim 10^{-11}$ Torr) single-probe scanning probe microscope (USM-1300, magnetic field up to 15 T) from UNISOKU. The STM tips were obtained by chemical etching from a wire of Pt(80%) Ir(20%) alloys. Lateral dimensions observed in the STM images were calibrated using a standard graphene lattice as well as a Si (111)-(7 \times 7) lattice. The STS

spectra were calibrated using a Ag(111) surface. The STS spectrum (the $dI/dV-V$ curve) was carried out with a standard lock-in technique by applying a 793 Hz alternating current modulation of the bias voltage of 5 mV to the tunneling bias.

■ ASSOCIATED CONTENT

SI Supporting Information

The Supporting Information is available free of charge at <https://pubs.acs.org/doi/10.1021/acs.nanolett.2c04710>.

Detailed analysis of the moiré magnifying lens, supplementary STS spectra, supplementary STM images, and theoretical calculations (PDF)

■ AUTHOR INFORMATION

Corresponding Authors

Ya-Ning Ren – Center for Advanced Quantum Studies, Department of Physics, Beijing Normal University, Beijing 100875, People's Republic of China; Email: yning@mail.bnu.edu.cn

Lin He – Center for Advanced Quantum Studies, Department of Physics, Beijing Normal University, Beijing 100875, People's Republic of China; orcid.org/0000-0001-5251-1687; Email: helin@bnu.edu.cn

Authors

Zhen Zhan – Key Laboratory of Artificial Micro- and Nano-structures of the Ministry of Education and School of Physics and Technology, Wuhan University, Wuhan 430072, People's Republic of China

Yi-Wen Liu – Center for Advanced Quantum Studies, Department of Physics, Beijing Normal University, Beijing 100875, People's Republic of China

Chao Yan – Center for Advanced Quantum Studies, Department of Physics, Beijing Normal University, Beijing 100875, People's Republic of China

Shengjun Yuan – Key Laboratory of Artificial Micro- and Nano-structures of the Ministry of Education and School of Physics and Technology, Wuhan University, Wuhan 430072, People's Republic of China; Wuhan Institute of Quantum Technology, Wuhan 430206, People's Republic of China; orcid.org/0000-0001-6208-1502

Complete contact information is available at: <https://pubs.acs.org/doi/10.1021/acs.nanolett.2c04710>

Notes

The authors declare no competing financial interest.

■ ACKNOWLEDGMENTS

This work was supported by the National Key R and D Program of China (Grant Nos. 2021YFA1401900, 2021YFA1400100, 2017YFA0303301, and 2018YFA0305800) and National Natural Science Foundation of China (Grant Nos. 12141401, 11974050, 11921005, 11974263, 12047543). Numerical calculations presented in this paper were performed on the supercomputing system in the Supercomputing Center of Wuhan University.

■ REFERENCES

(1) Geim, A. K.; Grigorieva, I. V. Van der Waals heterostructures. *Nature* **2013**, *499*, 419–425.

(2) Novoselov, K. S.; Mishchenko, A.; Carvalho, A.; Castro Neto, A. H. 2D materials and van der Waals heterostructures. *Science* **2016**, *353*, aac9439.

(3) Balents, L.; Dean, C. R.; Efetov, D. K.; Young, A. F. Superconductivity and strong correlations in moiré flat bands. *Nat. Phys.* **2020**, *16*, 725–733.

(4) Andrei, E. Y.; MacDonald, A. H. Graphene bilayers with a twist. *Nat. Mater.* **2020**, *19*, 1265–1275.

(5) Ren, Y.-N.; Zhang, Y.; Liu, Y.-W.; He, L. Twistronics in graphene-based van der Waals structures. *Chin. Phys. B* **2020**, *29*, 117303.

(6) Woods, C. R.; et al. Commensurate–incommensurate transition in graphene on hexagonal boron nitride. *Nat. Phys.* **2014**, *10*, 451–456.

(7) van Wijk, M. M.; Schuring, A.; Katsnelson, M. I.; Fasolino, A. Relaxation of moiré patterns for slightly misaligned identical lattices: graphene on graphite. *2D Mater.* **2015**, *2*, 034010.

(8) Dai, S.; Xiang, Y.; Srolovitz, D. J. Twisted Bilayer Graphene: Moiré with a Twist. *Nano Lett.* **2016**, *16*, 5923–5927.

(9) Gargiulo, F.; Yazyev, O. V. Structural and electronic transformation in low-angle twisted bilayer graphene. *2D Mater.* **2018**, *5*, 015019.

(10) Zhang, K.; Tadmor, E. B. Structural and electron diffraction scaling of twisted graphene bilayers. *J. Mech. Phys. Solids* **2018**, *112*, 225–238.

(11) Huang, S.; et al. Topologically Protected Helical States in Minimally Twisted Bilayer Graphene. *Phys. Rev. Lett.* **2018**, *121*, 037702.

(12) Qiao, J.-B.; Yin, L.-J.; He, L. Twisted graphene bilayer around the first magic angle engineered by heterostrain. *Phys. Rev. B* **2018**, *98*, 235402.

(13) Walet, N. R.; Guinea, F. The emergence of one-dimensional channels in marginal-angle twisted bilayer graphene. *2D Mater.* **2020**, *7*, 015023.

(14) Nam, N. N. T.; Koshino, M. Lattice relaxation and energy band modulation in twisted bilayer graphene. *Phys. Rev. B* **2017**, *96*, 075311.

(15) Yoo, H.; et al. Atomic and electronic reconstruction at the van der Waals interface in twisted bilayer graphene. *Nat. Mater.* **2019**, *18*, 448–453.

(16) Carr, S.; Fang, S.; Zhu, Z.; Kaxiras, E. Exact continuum model for low-energy electronic states of twisted bilayer graphene. *Phys. Rev. Research* **2019**, *1*, 013001.

(17) Fang, S.; Carr, S.; Zhu, Z.; Massatt, D.; Kaxiras, E. Angle-Dependent Ab initio Low-Energy Hamiltonians for a Relaxed Twisted Bilayer Graphene Heterostructure. 2019. arXiv: 1908.00058. <https://arxiv.org/abs/1908.00058> (accessed 2019-07-31).

(18) Rosenberger, M. R.; et al. Twist Angle-Dependent Atomic Reconstruction and Moiré Patterns in Transition Metal Dichalcogenide Heterostructures. *ACS Nano* **2020**, *14*, 4550–4558.

(19) Weston, A.; et al. Atomic reconstruction in twisted bilayers of transition metal dichalcogenides. *Nat. Nanotechnol.* **2020**, *15*, 592–597.

(20) Gornostyrev, Y. N.; Katsnelson, M. I. Origin of the vortex displacement field in twisted bilayer graphene. *Phys. Rev. B* **2020**, *102*, 085428.

(21) Liu, Y.-W.; et al. Tunable Lattice Reconstruction, Triangular Network of Chiral One-Dimensional States, and Bandwidth of Flat Bands in Magic Angle Twisted Bilayer Graphene. *Phys. Rev. Lett.* **2020**, *125*, 236102.

(22) Kazmierczak, N. P.; et al. Strain fields in twisted bilayer graphene. *Nat. Mater.* **2021**, *20*, 956–963.

(23) Zheng, Q.; Hao, C.-R.; Zhou, X.-F.; Zhao, Y.-X.; He, J.-Q.; He, L. Tunable sample-wide electronic Kagome lattice in low-angle twisted bilayer graphene. *Phys. Rev. Lett.* **2022**, *129*, 076803.

(24) N'Diaye, A. T.; et al. Structure of epitaxial graphene on Ir(111). *New J. Phys.* **2008**, *10*, 043033.

(25) Jiang, Y.; Mao, J.; Duan, J.; Lai, X.; Watanabe, K.; Taniguchi, T.; Andrei, E. Y. Visualizing strain-induced pseudomagnetic fields in

graphene through an hBN magnifying glass. *Nano Lett.* **2017**, *17*, 2839.

(26) Wong, D.; et al. Local spectroscopy of moiré-induced electronic structure in gate-tunable twisted bilayer graphene. *Phys. Rev. B* **2015**, *92*, 155409.

(27) Li, G.; et al. Observation of Van Hove singularities in twisted graphene layers. *Nat. Phys.* **2010**, *6*, 109.

(28) Luican, A.; et al. Single-layer behavior and its breakdown in twisted graphene layers. *Phys. Rev. Lett.* **2011**, *106*, 126802.

(29) Brihuega, I.; et al. Unraveling the Intrinsic and Robust Nature of van Hove Singularities in Twisted Bilayer Graphene by Scanning Tunneling Microscopy and Theoretical Analysis. *Phys. Rev. Lett.* **2012**, *109*, 196802.

(30) Yan, W.; et al. Angle-dependent van Hove singularities in a slightly twisted graphene bilayer. *Phys. Rev. Lett.* **2012**, *109*, 126801.

(31) Ohta, T.; et al. Evidence for Interlayer Coupling and Moiré Periodic Potentials in Twisted Bilayer Graphene. *Phys. Rev. Lett.* **2012**, *109*, 186807.

(32) Zuo, W.-J.; et al. Scanning tunneling microscopy and spectroscopy of twisted trilayer graphene. *Phys. Rev. B* **2018**, *97*, 035440.

(33) Turkel, S.; Swann, J.; Zhu, Z.; Christos, M.; Watanabe, K.; Taniguchi, T.; Sachdev, S.; Scheurer, M. S.; Kaxiras, E.; Dean, C. R.; Pasupathy, A. N. Orderly disorder in magic-angle twisted trilayer graphene. *Science* **2022**, *376*, 193.

(34) Zhu, Z.; Cazeaux, P.; Luskin, M.; Kaxiras, E. Modeling mechanical relaxation in incommensurate trilayer van der Waals heterostructures. *Phys. Rev. B* **2020**, *101*, 224107.

(35) Yin, L.-J.; Qiao, J.-B.; Wang, W.-X.; Zuo, W.-J.; Yan, W.; Xu, R.; Dou, R.-F.; Nie, J.-C.; He, L. Landau quantization and Fermi velocity renormalization in twisted graphene bilayers. *Phys. Rev. B* **2015**, *92*, 201408R.

(36) Zhao, Y.-X.; Zhou, X.-F.; Zhang, Y.; He, L. Oscillations of the spacing between van Hove singularities induced by sub-Angstrom fluctuations of interlayer spacing in graphene superlattices. *Phys. Rev. Lett.* **2021**, *127*, 266801.

(37) Huder, L.; et al. Electronic spectrum of twisted graphene layers under heterostrain. *Phys. Rev. Lett.* **2018**, *120*, 156405.

(38) Mesple, F.; et al. Heterostrain determines flat bands in magic-angle twisted graphene layers. *Phys. Rev. Lett.* **2021**, *127*, 126405.

(39) Zhang, Y.; et al. Correlation-induced valley splitting and orbital magnetism in a strain-induced zero-energy flatband in twisted bilayer graphene near the magic angle. *Phys. Rev. B* **2020**, *102*, 081403R.

(40) Ju, L.; et al. Topological valley transport at bilayer graphene domain walls. *Nature* **2015**, *520*, 650–655.

(41) Yin, L.-J.; Jiang, H.; Qiao, J.-B.; He, L. Direct imaging of topological edge states at a bilayer graphene domain wall. *Nat. Commun.* **2016**, *7*, 11760.

(42) Ren, Y.-N.; Cheng, Q.; Sun, Q.-F.; He, L. Realizing valley-polarized energy spectra in bilayer graphene quantum dots via continuously tunable Berry phases. *Phys. Rev. Lett.* **2022**, *128*, 206805.

(43) Ramires, A.; Lado, J. L. Electrically Tunable Gauge Fields in Tiny-Angle Twisted Bilayer Graphene. *Phys. Rev. Lett.* **2018**, *121*, 146801.

Recommended by ACS

Observation of Gapped Topological Surface States and Isolated Surface Resonances in PdTe₂ Ultrathin Films

Jacob Cook, Guang Bian, *et al.*

FEBRUARY 24, 2023
NANO LETTERS

READ 

Ferrocic Berry Curvature Dipole in a Topological Crystalline Insulator at Room Temperature

Taiki Nishijima, Masashi Shiraishi, *et al.*

MARCH 01, 2023
NANO LETTERS

READ 

60 nm Span Wavelength-Tunable Vortex Fiber Laser with Intracavity Plasmon Metasurfaces

Lili Gui, Kun Xu, *et al.*

FEBRUARY 15, 2023
ACS PHOTONICS

READ 

Switchable Unidirectional Radiation from Huygens Dipole Formed at an Exceptional Point in Non-Hermitian Plasmonic Systems

Yuto Moritake and Masaya Notomi

FEBRUARY 24, 2023
ACS PHOTONICS

READ 

Get More Suggestions >